SCATTERING CORRECTION THROUGH A SPACE-VARIANT BLIND DECONVOLUTION ALGORITHM

Koberstein-Schwarz B.[1,2], Omlor L.[1], Mappes T.[1], Ntziachristos V.[2]

[1] *Carl Zeiss AG, Corporate Research & Technology, Carl-Zeiss-Promenade 10, 07745 Jena, Germany*

[2] *Institute for Biological and Medical Imaging (IBMI), Technische Universität München and Helmholtz Zentrum, München, Ingolstädter Landstrasse 1, 85764 Neuherberg, Germany*

ABSTRACT

Scattering within biological samples is limiting the imaging depth and the resolution in microscopy. In this work an algorithm is introduced to correct for the influence of scattering in order to significantly increase the imaging depth and resolution. To demonstrate the function of the algorithm a 3D image stack of a zebrafish embryo captured with a selective plane illumination microscope (SPIM) is used. The method is based on a space-variant blind deconvolution algorithm. Image information from adjacent z-planes is applied to estimate the unknown blur in tissue. A new regularizer models the increasing width of the point spread function and enables coping with the increase in blur observed due to scattering in deeper tissue. The point in depth where scattering has a significant effect on the image quality could be extended by around 30 µm.

INTRODUCTION

One of the most prominent limitations for light microscopy of biological samples is the imaging depth. Scattering in tissue is the limiting factor defining the depth in which biological structures still may be resolved. There are different approaches to overcome this limitation. On one side the sample can be adapted to be more transparent either by the usage of (genetically engineered) transparent organisms[1,2], or by treating the sample with clearing chemicals[3,4]. While the usage of transparent organisms is limited to a few (small) model organisms and solely defined stages of their developement, chemical clearing can only be performed ex-vivo.

On the other side advanced microscopy methods are pushing the imaging depth further and enable 3D in-vivo imaging. Common methods applied are e.g. beam and wavefront shaping[5,6] as well as multi photon techniques to significantly increase the penetration depth[7].

One technique, which has arisen in the last decade, is selective plane illumination microscopy (SPIM)[8–10]., Here, a fluorescent microscope is applying an extreme darkfield setup by illuminating the focal plane in the sample by a light sheet only. The illumination is usually positioned perpendicular to the detection objective. By scanning the sample through the light sheet a 3D image stack of the sample can be acquired in a rather short period of time. The microscope offers a high acquisition rate of whole volumes and low photo damage and bleaching, therefore making it an ideal tool for in-vivo imaging of

fast processes or developing organisms. While the confocal principle used in SPIM helps to alleviate the problem of scattering, it is still the limiting resolution factor. Multi-view reconstruction algorithms[11,12] can extent the imaging depth of SPIM. The drawback for multi-view based reconstruction is the long acquisition time required to capture image stacks from multiple directions. Therefore a huge advantage of SPIM, the fast imaging ability, is lost.

In this work a reconstruction algorithm is presented, which is not based on multiple view (although it can be extended to fuse multi-view data). To correct for scattering the algorithm implements a straight-forward scattering model while using the information within one image stack only.

THEORY

The scattering influence on intensity within a sample can be treated as a convolution between the real object and an increasingly broad point spread function. More generally speaking the point spread function (PSF) describes the effect an imaging system has on a point source. For SPIM this PSF has three different contributions: (1) the illumination function of the sample. The shape of the light sheet as well as broadening of the light sheet within the sample due to scattering determines the illuminated areas of the sample. Only from these regions we can expect fluorescence. To acquire a whole 3D image of the sample the lightsheet and the sample are moved relative to each other. The direction of movement will be denoted as z-direction, while the imaging plane will be labeled x-y-plane. The function describing the illumination will be called P_{illum}. (2) Fluorescence molecules, which are illuminated in the current z-position, can be considered as a point source. The light from these sources gets scattered on the way to the objective, which will broaden the PSF P_{scatt} and will contribute to the overall PSF. (3) Eventually the detection optics contribute to the PSF. This contribution P_{det} is sample independent and for most cases smaller than the PSF broadening due to scattering. In the following all three separate contributions are condensed in one single PSF.

$$I_{z_0}(x,y) = \left(\int O(x,y,z) P_{illum}(z - z_0) P_{scatt}(x,y,z,z_0) \mathrm{d}x\mathrm{d}y\mathrm{d}z\right) * P_{det}$$

Spatially invariant algorithm

For the sake of clarity the algorithmic details are first discussed using a spatially invariant model. In each z-plane the detected SPIM image is treated as a convolution between the real object and the point spread function (PSF). In this case the real object is the distribution of fluorophores in the sample. An additional noise-term accounts for all the noise influences on the final image introduced by the imaging system:

$$\boldsymbol{I_z = O_z * P_z + N} \qquad (1)$$

Here N is the noise, I is the image, O is the real object and P is the PSF. If N is Gaussian noise than the original image can be estimated by minimizing the least square error E.

$$E = \|I - P * O\|_2^2$$

Since only I is known in this equation it is typically ill conditioned. Trying to minimize the least square error will not necessarily converge to one solution. To get a converging solution further assumptions have to be made. The main assumption for this algorithm is, that if the step size between two consecutive z-planes is small enough it can be assumed that the same object is illuminated in both positions, while the PSF will slightly change. Under ideal conditions and the assumption of multiple observations P_i $(i = 1,2,3)$ the co-primeness equation: $P_j * I_i - P_i * I_j = 0 \; \forall \; i \neq j$ can be used to determine the PSF. In the presence of noise this equation becomes an optimization problem:

$$E_{coprime} = \sum_{i \neq j} \left|\left| P_j * I_i - P_i * I_j \right|\right|_2^2$$

Algorithms with are based on deconvolution and assume a constant object with a varying PSF have already been shown by several groups[13–15]. Due to the physical properties of the imaging system it can additionally be assumed that PSF $P \geq 0$, as well as $\sum_{x,y} P(x,y) = 1$.

The sum constraint is only valid if absorption in the sample can be neglected, which is reasonable concerning only adjacent z-planes. The positive constrain is also true for the object O. Furthermore the support of the PSF should be smaller than the image I. These constrains together with the assumptions that the object in the z-plane above and below is the same while the PSF P_i $(i = 1,2,3)$ changes lead to the following minimization problem:

$$\min_{P_i \geq 0, \sum P_i = 1, O \geq 0} \sum_i \|I_i - P_i * O\|_2^2 + \sum_{i \neq j} \left\| P_j * I_i - P_i * I_j \right\|_2^2$$

The last term, the comprimeness regularization mentioned above, helps to stabilize the deconvolution problem and can even lead to a unique solution[13].

To ensure the convergence of both, the PSF P and the object O an alternating optimization scheme is used, where the optimization iterates between P and O. In this work the optimization is done with an established non-negative least square estimator, the image space reconstruction algorithm (ISRA)[16–18]. In the first step the PSF is updated by applying the ISRA:

$$P_k(t+1) = P_k(t) \frac{O * O^* * I_k + \sum_{j \neq k} I_j * \; I_j^* * \; P_j(t) * I_k}{\left(O * O^* + \sum_{(j \neq k)} \mathrm{I_j} * \; \mathrm{I_j^*}\right) * \; P_k(t)}$$

In the second iteration step the PSF is fixed and the object is updated in the same way. To ensure convergence of both, the PSF and the object, a proximal minimization method is applied to the algorithm[19,20]

With increasing imaging depth the images will suffer from increased scattering. The idea in this work is to compensate for this increased scattering by adjusting the algorithm along with the imaging depth. A simple approximation for light scattering in tissue is found in [21,22]. With increasing depth the size of the PSF grows quadratically. This simple model was implemented by the use of the Tikhonov regularization[23]. A higher Tikhonov regularization leads to an increased PSF size in the reconstruction.

This is not an intrinsic effect of the regularization itself but an combination effect with the constant intensity constraint $\sum P_i = 1$. The ratio between the l1-norm (sum constraint) and the l2-norm (Tikhonov regularization) is a measure of signal sparsity with higher values describing sparser signals. Since the Tikhonov term reduces the l2-norm of the solution (this is penalized in the final cost function) the regularized solution has automatically a lower sparsity, i.e. has a larger support (broader blur).

To reflect the increase in the PSF size the regularization parameter was increased quadratically, which was empirically found to be an effective way to model the increased scattering.

Spatially varying algorithm

In general the scattering will not only vary with depth but will also depend on the x-y position within the sample. Hence equation (1) generalizes to:

$$I_z(x,y) = O(x,y,z) * P_z(x,y) + N$$

Space variant deconvolution has been successfully used by other authors to remove motion artefacts[24,25]. To account for this spatial dependency a Gabor transform was added to the algorithm to dived the original image into several smaller overlapping windows. The Gabor transform (GT_x) in this algorithm[26] is defined as: $GT_x(I) = \mathcal{F}(I * h(x)^{0.5})$, where $h(x)$ is the window function. In the presented algorithm a $\sin(x)^2$ is used to model the window. Consequentially the inverse transform is given with: $I = \sum \mathcal{F}^{-1}[GT_x(I)] \cdot h(x)^{0.5}$. The calculation of the object and the PSF is done for each of these windows and in the end the object is put back together with the inverse transform. The size of the windows was chosen to be large enough to most closely satisfy the $\sum P_i = 1$ constraint. Since the sample is not necessarily flat and the position of the sample surface might vary from window to window the depth regularization by the adapted Tikhonov parameter was done for each window independently. A threshold was used to locate the z-position of the sample surface and from there the depth was measured.

SIMULATION

To demonstrate the algorithm and to visualize its function the algorithm was first applied to a set of artificial data. The simulated data set was a volume with several overlapping cylinders. This original volume was convolved with an ellipsoidal PSF. Since the algorithm is based on variation in the PSF, the generated PSF was altered for each z-plane in the volume by quadratically increasing the width σ^2 of the PSF. An example of the generated PSF can be found in Figure 1b), where the PSF from z-plane 18 is shown. The convolved data set was then reconstructed by the introduced algorithm. In Figure 1 the results of the reconstruction can be found. Figure 1a) shows the mean square error (MSE) of the convolved and the reconstructed data set compared to the original volume as a function of depth (z-position). Three different planes (z=6, z=18, z=28) are marked in the graph and a cross section from these planes is shown in 1d)-f). The region where the cross section is taken from is identical for all three plot and is marked in 1g). All three images 1g)-i) show the reconstructed z-planes from the same depths as the cross sections above (z=6, z=18, z=28).

Although in this case no spastically varying PSF was used to create the artificial data set, the reconstruction algorithm was using 25 windows (the same amount to be used in the experimental

setup). The only parameter which had to be slightly adapted was the factor in front of the quadratically increasing regularization parameter.

Whereas in the beginning both the convolved data set and the reconstructed data set yield the same results, the edge steepness of the reconstructed data is decreasing much slower than the edge steepness of the convolved data. This can be seen in Figure 1d)-f) where the convolved data (colored in green) is compared to the reconstructed data (colored in red) as well as in Figure 1a) where the MSE of the reconstructed data (also colored in red) starts to rise later than the MSE of the convolved data (colored in green).

To further validate the function of the algorithm the calculated PSF is compared to the initial PSF. The initial or original PSF is known, since it was used to produce the artificial data set. One of the 25 PSFs of the different windows from plane z = 18 calculated by the algorithm can be seen in Figure 1c), next to the original PSF in Figure 1b). Although the original PSF shows a slightly higher intensity in the outer regions both PSF coincide well. The PSFs have the same directionality and about the same width.

The results from the simulated data set demonstrate the function of the algorithm. It is shown that the algorithm is able to improve the image quality for a volume with an increasing simulated scattering. Since constant cylinders over all z-planes were assumed in the simulation, it is not shown how the approximation of a constant object within the algorithm is affecting its function. To validate this approximation as well as to test the algorithm under real conditions a real data set is used in the following section.

EXPERIMENTS

We demonstrated the effect of the algorithm on a real dataset by choosing a common model organism for biological research, a transgenic zebrafish embryo. The 3 day old embryo of the type Fli1A had its vasculature labeled with EGFP. Imaging was done *ex-vivo* with SPIM. The fish was imaged sideways with a step size of 5 µm between the different z-planes. Two complete 3D image stacks of the zebrafish embryo were acquired, one stack from each side. While reconstruction was only performed on the first image stack (S1) the second image stack (S2) was used as a control image. Since the imaging was done from two opposed sites, structures which appear deep and scattered in S1 are better visible in S2. This circumstance is used to validate the reconstruction results from S1. Figure 2A shows a maximum intensity projection along the z-axis from the dataset S1. The orange marked area is used in the following to show the results of the reconstruction algorithm. The same orange marked area can also be found in Figure 2C, where the perpendicular maximum intensity projection along the y-axis of the same dataset S1 is shown. The image shows a top view of the zebrafish embryo. The left side is the front, facing the objective; the right side is the back of the fish. The width of the fish within the marked area is about 175 µm. The blue dashed line indicates one z-plane at 130 µm depth, measured from the front of the fish. Figure 2B shows images from three different depths: 105 µm, 130 µm, and 155 µm. For this sample, the depicted depths are just in the range where scattering starts to drastically reduce the image quality. In the left column the original dataset S1 can be found, the column in the middle shows the S1 dataset after it has been processed with the introduced algorithm, and the column to the right shows the dataset S2.

The section shown was reconstructed using 25 windows. Compared to the original dataset S1 the reconstructed dataset shows a clear improvement in image quality at a depth of 105 and 130 µm, respectively. The structures which can be seen in 105 µm depth at the bottom of the reconstructed image agree well with the structures in the second dataset S2. The effect is still visible at a depth of 130 µm. Going deeper into the sample the ability of the algorithm to correct the image will diminish. At a depth of 155 µm the image improvement is not able to reveal detailed structures anymore.

The results demonstrate the function of the algorithm on a stack of SPIM images, which does not mean that the algorithm is limited to this imaging modality. The algorithm should be able to work with other optical microscopy methods as well as other imaging methods which are limited by the scattering of light in tissue. The only requirements are that a whole 3D image stack is available, that the step size between two adjacent planes is small compared to the observed structures and that the scattering in the sample can be sufficiently described by the introduced model. While for this demonstration a single data set was used, the algorithm can be extended to handle multiple data sets to form one sample either with varying illumination or even with varying views of the sample.

CONCLUSION

Both the simulated results as well as the results from a real data set show the iterative algorithm presented in this work is able to correct for scattering within the sample and enhance the image quality and depth about 30 µm. For this correction only information from a single image stack was used, together with a simple model for the dispersive broadening of light in tissue. Tikhonov regularization is used efficiently as a model to account for an increased scattering which comes along with an increased imaging depth. The advantage of this approach is that neither multiple image stacks have to be acquired, nor adaptions on the hardware level are required and the algorithm can be applied to already acquired data. The algorithm only requires a volumetric image stack with a small step size between two adjacent imaging planes, therefore the algorithm should also be able to work on other imaging techniques which provide a 3D image volume.

ACKNOWLEDGEMENT

We would like to thank Tobias Schmitt-Manderbach from Zeiss for designing and building the SPIM system. The work has received funding from the Federal Ministry of Education and Research (BMBF), Photonic Science Germany, Tech2See-13N12623 /-4.

BIBLIOGRAPHY

1. Haffter, P. *et al.* The identification of genes with unique and essential functions in the development of the zebrafish, Danio rerio. *Development* **123,** 1–36 (1996).

2. Kaletta, T. & Hengartner, M. O. Finding function in novel targets: C. elegans as a model organism. *Nat. Rev. Drug Discov.* **5,** 387–398 (2006).

3. Tuchin, V. V. Optical clearing of tissues and blood using the immersion method. *J. Phys. D. Appl. Phys.* **38,** 2497–2518 (2005).

4. Ke, M., Fujimoto, S. & Imai, T. SeeDB : a simple and morphology-preserving optical clearing agent for neuronal circuit reconstruction. *Nat. Publ. Gr.* **16,** 1154–1161 (2013).

5. Chaigne, T., Gateau, J., Katz, O., Bossy, E. & Gigan, S. Light focusing and two-dimensional imaging through scattering media using the photoacoustic transmission matrix with an ultrasound array. *Opt. Lett.* **39,** 2664–2667 (2014).

6. Vellekoop, I. M. & Mosk, A. P. Focusing coherent light through opaque strongly scattering media. *Opt. Lett.* **32,** 2309–2311 (2007).

7. Hoover, E. & Squier, J. Advances in multiphoton microscopy technology. *Nat. Photonics* **7,** 93–101 (2013).

8. Huisken, J., Swoger, J. & Bene, F. Del. Optical sectioning deep inside live embryos by selective plane illumination microscopy. *Science (80-.).* **1007,** (2004).

9. Huisken, J. & Stainier, D. Y. R. Selective plane illumination microscopy techniques in developmental biology. *Development* **136,** 1963–75 (2009).

10. Keller, P., Schmidt, A., Wittbrodt, J. & Stelzer, E. Reconstruction of zebrafish early embryonic development by scanned light sheet microscopy. *Science (80-.).* **322,** 1065–1069 (2008).

11. Krzic, U., Gunther, S., Saunders, T. E., Streichan, S. J. & Hufnagel, L. Multiview light-sheet microscope for rapid in toto imaging. *Nat. Methods* **9,** 730–3 (2012).

12. Preibisch, S. *et al.* Efficient Bayesian-based multiview deconvolution. *Nat. Methods* **11,** 645–8 (2014).

13. Harikumar, G. & Bresler, Y. Perfect blind restoration of images blurred by multiple filters: theory and efficient algorithms. *IEEE Trans. Image Process.* **8,** 202–19 (1999).

14. Sroubek, F. & Flusser, J. Multichannel blind iterative image restoration. *IEEE Trans. Image Process.* **12,** 1094–106 (2003).

15. Sroubek, F. & Flusser, J. Multichannel blind deconvolution of spatially misaligned images. *IEEE Trans. Image Process.* **14,** 874–83 (2005).

16. Lanteri, H., Soummer, R. & Aime, C. Comparison between ISRA and RLA algorithms. Use of a Wiener Filter based stopping criterion. *Astron. Astrophys. Suppl. Ser.* **140,** 235–246 (1999).

17. Archer, G. & Titterington, D. The iterative image space reconstruction algorithm (ISRA) as an alternative to the EM algorithm for solving positive linear inverse problems. *Stat. Sin.* **5,** 77–96 (1995).

18. Reader, A. Generalization of the image space reconstruction algorithm. *Nucl. Sci. Symp. Conf. Rec.* 4233–4238 (2011).

19. Bertsekas, D. P. On penalty and multiplier methods for constrained minimization. *SIAM J. Control Optim.* **14,** 216–235 (1976).

20. Bertsekas, D. P. & Tsitsiklis, J. N. *Parallel and distributed computation: numerical methods*. **23,** (1989).

21. Premože, S. & Ashikhmin, M. Practical rendering of multiple scattering effects in participating media. *Eurographics Symp. Render.* (2004).

22. McLean, J. W., Freeman, J. D. & Walker, R. E. Beam spread function with time dispersion. *Appl. Opt.* **37,** 4701–11 (1998).

23. Benvenuto, F. & Piana, M. Regularization of constrained maximum likelihood iterative algorithms by means of statistical stopping rule. *arXiv Prepr. arXiv1212.3258* 20 (2012).

24. Hirsch, M., Sra, S., Schölkopf, B. & Harmeling, S. Efficient filter flow for space-variant multiframe blind deconvolution. *CVPR* (2010).

25. Harmeling, S., Hirsch, M. & Schölkopf, B. Space-Variant Single-Image Blind Deconvolution for Removing Camera Shake. *NIPS* 1–9 (2010).

26. Lamoureux, M. & Gibson, P. A fast, discrete Gabor transform via a partition of unity. 1–37 (2003).

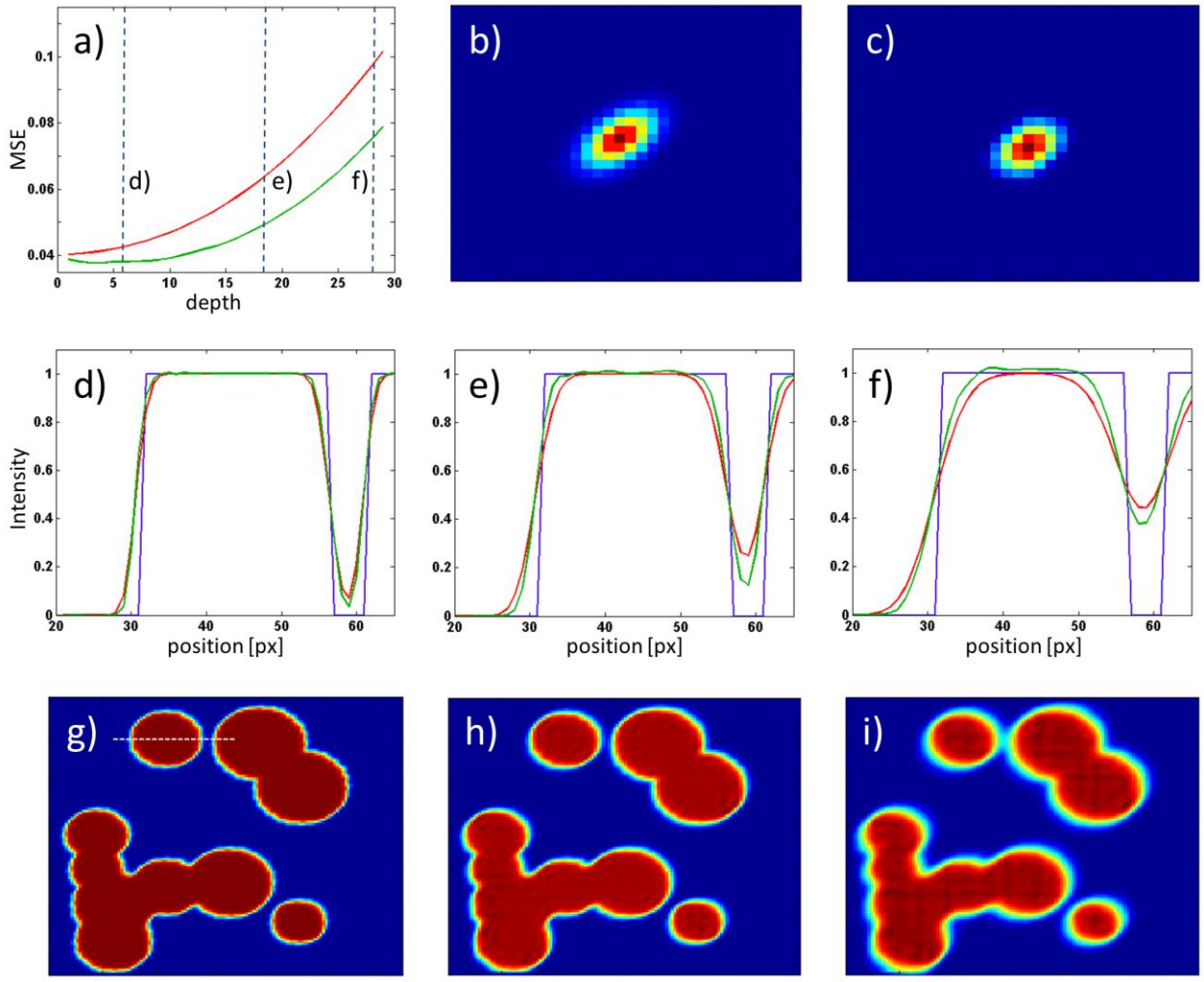

Figure 1: a) Mean square error of the artificial data set (colored in green) and its reconstruction (colored in red) as a function of depth (z-position). The three dashed lines indicate the depth at which the images as well as the cross sections were taken. b) PSF which is used to generate the artificial data set for the depth z=18; c) Reconstructed PSF from the same depth z=18; d)-f) cross sections through different z-planes: d) z=6, e) z=18, f) z=28. In blue the original object is plotted, in green the convolved object, or the simulated data set is shown and in the red the reconstructed data set can be seen. g)-i) z-planes corresponding to the depth of the cross sections above: g) z=6, h) z=18, i) z=28. The white dotted line in g) indicates the position the cross sections were taken from. The images with is 256 px.

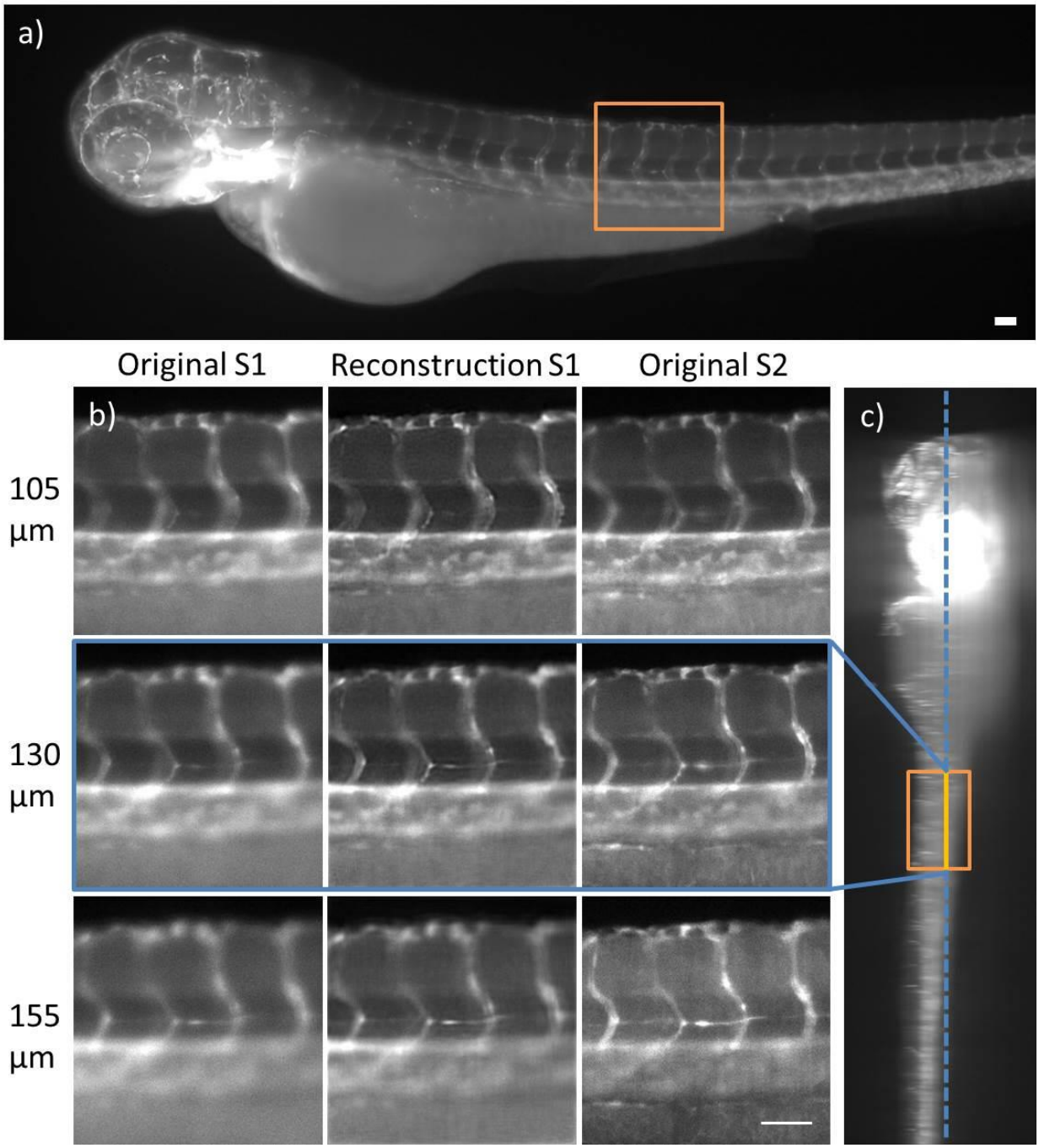

Figure 2: a) Maximum intensity projection (MIP) of the used data set (S1). The image shows a zebrafish from the genetic line Fli1A 3 days past fertilization. The orange-colored box indicated the region which was used to demonstrate the reconstruction algorithm. b) The lines show the same region at different depth (105 µm, 130 µm, 155 µm). The column on the left shows the original data set (S1), the column in the middle shows the reconstruction of the data set to the left and the column on the right side shows a second data set (S2), which was recorded from the opposite side of the fish to validate the reconstruction results. c) MIP of S1 this time from the top to the bottom of the fish. The left side of the fish is considered to be the front. The depth is therefore measured from left to right. The orange box again marks the region of interest. The blue dashed line indicates the z-plane shown in the middle line in b). Scale bar indicates 100 µm